nature research

https://doi.org/10.1038/s41567-020-01098-8

Supplementary information

Vibrational coherent control of localized *d*–*d* electronic excitation

In the format provided by the authors and unedited

Vibrational coherent control of localized d-d electronic excitation Supplementary Information

Alexandre Marciniak[1,2,⋆], Stefano Marcantoni[1,3,⋆], Francesca Giusti[1,2], Filippo Glerean[1,2], Giorgia Sparapassi[1,2], Tobia Nova[5], Andrea Cartella[5], Simone Latini[5], Francesco Valiera[1], Angel Rubio[5], Jeroen van den Brink[4], Fabio Benatti[1,3], and Daniele Fausti[1,2,6,†]

[1] *Department of Physics, University of Trieste, Via A. Valerio 2, 34127 Trieste, Italy*
[2] *Elettra-Sincrotrone Trieste S.C.p.A. Strada Statale 14 - km 163.5 in AREA Science Park 34149 Basovizza, Trieste, Italy*
[3] *National Institute for Nuclear Physics (INFN), Trieste Section, I-34151, Trieste, Italy*
[4] *Leibniz Institute for Solid State and Materials Research IFW, 01069 Dresden, Germany*
[5] *Max Planck Institute for the Structure and Dynamics of Matter, Hamburg, Germany*
[6] *Department of Chemistry, Princeton University, Princeton, New Jersey 08544, United States*
[⋆] *Those authors have contributed equally to this work*
[†] *Corresponding author : daniele.fausti@elettra.eu*

1 Experimental details

1.1 $CuGeO_3$ optical properties

Copper Germanate ($CuGeO_3$, see Fig.1.c) is a model edge-sharing cuprate known for his spin-Peierls transition near 14K [1]. It is composed by chains of Copper-Oxygen octahedral structures whose direction corresponds to the c-axis of the crystal. In this study, we have used a 100 μm thick sample of single crystal $CuGeO_3$ (provided by A. Revcolevschi). The results along the c-axis are presented in the main article and few ones about the b-axis are presented in this supplementary.

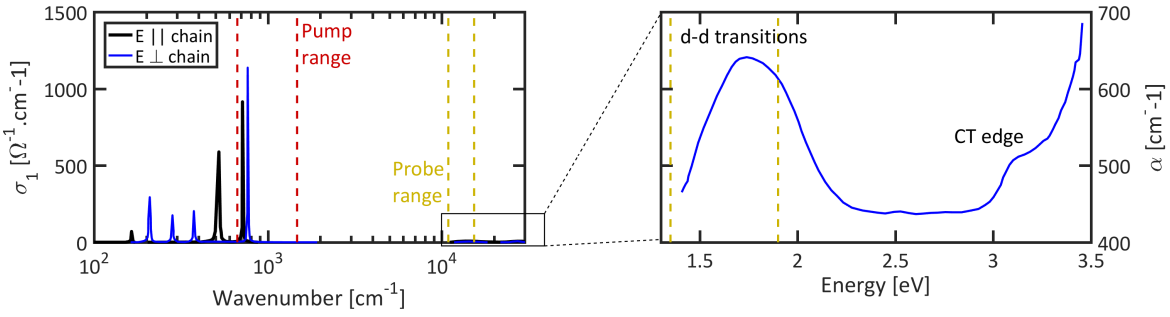

Figure 1: (Left) Optical conductivity of $CuGeO_3$ for two polarizations: along the c-axis (parallel to the chain) or the b-axis (perpendicular to the chain). The pump (resp. probe) wavelength range is indicated by red (resp. orange) dashed line. (Right) Zoom on the electronic transitions which shows that the d-d transitions are split from higher electronic transitions. Data issued from [2, 5].

For the purpose of this study, it is also interesting to detail the optical properties of $CuGeO_3$. Indeed, it owns many intense phonon modes at low energy [2, 3] (Supplementary Fig.1-left) and a group of

three phonon-assisted d-d transitions that is isolated in energy from other electronic transitions (Supp. Fig. 1-right). These properties are suitable if one wants to excite specific low energy modes and to probe the response of the three d-d transitions, located between 1.5 and 2 eV, independently from the response of other electronic transitions.

1.2 Scheme of principle of the experimental setup (Figure 2)

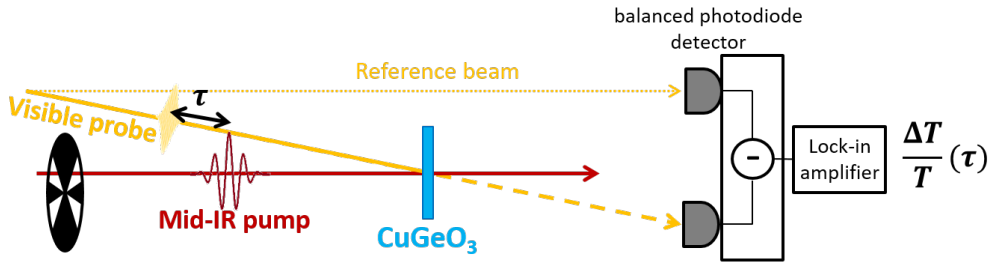

Figure 2: Scheme of the experimental setup used to measure the transient transmissivity with an accuracy down to 10^{-5}.

1.3 Analysis

Zero delay shifts. Due to technical details related with the NOPA-design, it was not possible to keep a constant zero delay while changing the probe wavelength. Thus, for each probe wavelength, the zero delay has been fixed in a post-measurement treatment. In particular, it has been chosen as the starting point of the dynamics, i.e. the beginning of the decreasing or increasing edge of ΔT/T. This choice is justified if we assume that the mechanism leading to the decrease or the increase of ΔT/T is "suddenly" triggered by the pump pulse, in other words, if there is no delay between the variation of ΔT/T and the true excitation moment. If so, the ΔT/T decreasing (resp. increasing) edge is fixed by the cross-correlation duration between the pump and the probe. In our case, the probe duration is much shorter than the pump duration (30 fs comparing to 260 fs), therefore the ΔT/T dynamics edge corresponds to the delay when both pulses start to interact which is then chosen as the "zero delay".

Fitting procedure. As described in the Methods, we have performed a fit of the measured response in the energy-domain and we have repeated this fit for each time delay. In particular, we have firstly fitted the optical absorption of the d-d transitions (linear response), which has been measured by O'Neal et al. [4], by three Gaussians plus a background in order to obtain a set of initial parameters. We want to emphasize that we have tried other distributions to fit this optical absorption, especially by using Lorentzian shapes or Fano profiles. However, using Gaussian distributions seems to be the most reproducible and stable manner of fitting the data, i.e. the less sensitive one to initial guess of the parameters. Note also that it might be probable that a non-trivial kind of distribution could correspond to the absorption shape of these phonon-assisted transitions. Indeed, we have shown, through a minimalist model (see 3.3 Supp. Fig.8), that the distribution shape could rather be similar to a "full and displaced" Maxwell-Boltzmann distribution[1] whose central energy is the one of the d-d transition. Obviously, this kind of distribution has the drawback to be hard to interpret whereas

[1]By "full", we mean that we include the positive and negative part of a typical Maxwell-Boltzmann distribution of type $p(E) \propto \frac{E^2}{\sigma_E^3} exp(-\frac{E^2}{2\sigma_E^2})$. By "displaced", we mean that the energy axis has to be shifted in such a way that E is replaced by $E' = E - \epsilon$ in the previous formula.

the Gaussian distribution parameters are easily intelligible. Therefore, we have used the extracted parameters from the Gaussian fits of the linear response as input parameters to construct a fitting function for the transient transmissivity map which results are plotted in Supp. Fig. 3. The evolution of each Gaussian parameter is plotted in Supp. Fig. 3.e and we can observe that it is possible to differentiate the response of each transition since the variation of the amplitudes are dynamically specific. Moreover, for the first d-d transition, the best way to fit the observed transient transparency is to let free the central energy and bandwidth of the transition (E_1 and σ_1). Note that the background constant (BG) has to evolve in order to reproduce the low energy features (below 1.45 eV). We interpret this as if an ingredient was missing in the chosen distribution used to fit the linear response. Indeed, we could imagine that a realistic distribution could have some contributions in an energy range out of the measured features of the d-d transitions. Even if this point remains unclear, we can however claim that the lowest energy observed dynamics is induced by the coherent midIR excitation since it is not only negative as it was the case in previous studies [5, 6].

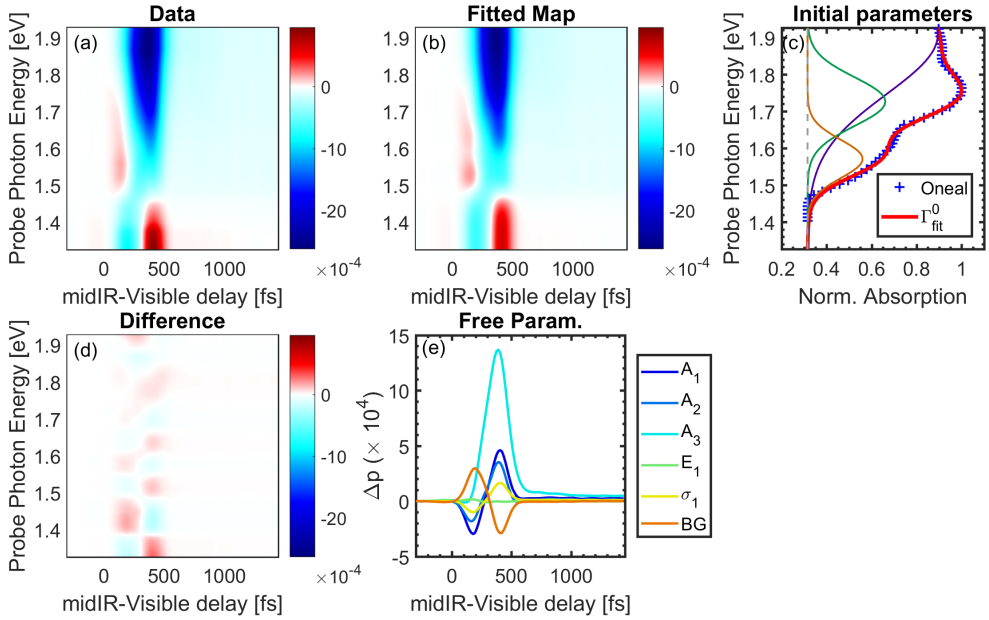

Figure 3: (a) Measured data same as in the main article Fig.2. (b) Retrieved fitted map obtained by varying the extracted parameters of the (c) fit with three Gaussians of the optical absorption (adapted from [4]. (d) Difference between the data and the fitted map in order to appreciate the quality of the fit. (e) Variation of the free parameters used in (b).

2 Complementary results and discussion

2.1 Thermal effects

Effects of the sample initial temperature. The $CuGeO_3$ d-d transitions have a strong dependence as a function of the temperature. In particular, the d-d absorption amplitude increases when the temperature increases and we can justify this behavior thanks to the developed theoretical model (see. section 3). Besides, all the d-d transitions shift towards lower energies at higher temperatures (see Supplementary Fig.4.a) and they also broaden in the linear response case. Therefore, we also wanted to study the effects of the sample initial temperature on the transient response of the d-d

transitions. These results are shown in Supplementary Fig.4.b-c, where we compare two transient maps measured at 8 K and 300 K, in the same pump and probe conditions ($\lambda_{pump} = 9\mu$m). We can observe that, at 300 K, the transient signal is very similar (in time and amplitude) to the one at 8 K but it has been shifted towards lower energy. We have also plotted some colored lines that indicate the central energy of the fitted Gaussians in both cases. The energy shift of the overall map is similar to the one that is observable in the linear absorption response case (about 60 meV), which supports the idea of midIR-induced distortions that would similarly impact the d-d transitions whatever the temperature is. It notably opens the perspectives in providing a way to induce some specific electronic properties at room temperature. Finally, note that $CuGeO_3$ has a Spin-Peierls transition around 14 K but no particular signature of this transition has been observed in this experiment.

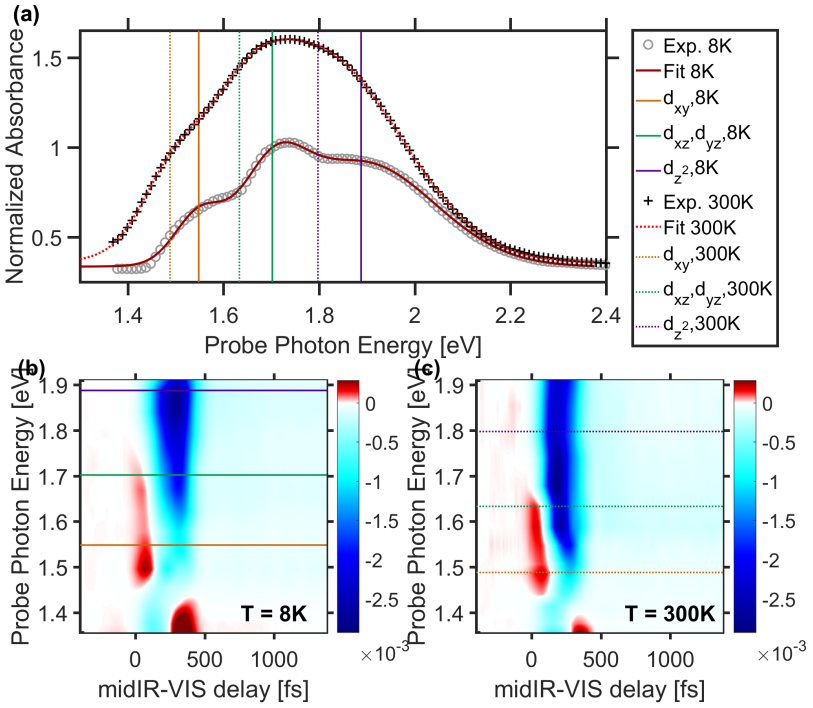

Figure 4: (a) Linear absorption measurements adapted from [4] at 8 K (gray circle) and 300 K (black cross) and their respective fit (plain dark red at 8K, dashed red at 300K). As a guide for the eyes, we have also plotted the central energy of the 3 fitted Gaussians representing the 3 d-d transitions. (b-c) Transmissivity maps at 8 K and 300 K for the same conditions of pump and probe beams.

Pump-induced thermal effects As discussed in the main text, it is important to estimate the possible temperature increase due to the pump excitation in order to understand its potential role in the transmissivity maps. For that purpose, we have considered that the absorbed energy from the pump (ΔQ_{pump}) is transferred into heat, which allows defining the temperature increase as:

$$\delta T = \frac{\Delta Q_{pump}}{C_T \times n_{CuGeO_3}}, \begin{cases} \Delta Q_{pump} = FS(1-R-T) \quad in\,[J] \\ n_{CuGeO_3} = \dfrac{S \times L}{V_{cell} \times N_A} \quad in\,[mol] \end{cases} \tag{1}$$

where F is the midIR fluence (1 mJ.cm^{-2}), S is the focus area (disk of radium $r = 75\mu$m), R is the reflection on the surface ($\simeq 6.5\%$ at 9μm [2]), T is the transmission coefficient (see below, eq.2), L

is the sample thickness (100μm), V_{cell} is the volume of one $CuGeO_3$ unit cell (59.9Å^3), N_A is the Avogadro constant and C_T is the heat capacity (0.43 J.K^{-1}.mol^{-1} at 8 K [7], and 100 J.K^{-1}.mol^{-1} at 300 K[8]). To compute ΔQ_{pump}, one needs the transmission coefficient which can be measured (not done in this study) or computed by the following standard formula [9] :

$$T = \frac{(1-R)^2 exp(-\alpha_\lambda L_{sample})}{1 + R^2 exp(-2\alpha_\lambda L_{sample})} \tag{2}$$

where α_λ is the absorption coefficient which depends on the wavelength. Then, we base our reasoning on the measurements of R and T of ref. [2] on a very broad spectral range. They have found $R = 0.065$ and $T = 0.78$ at $\lambda = 9\mu$m which gives, thanks to eq.2, $\alpha_{9\mu m} L_{sample} \simeq 0.11$. As they did not specify their sample thickness, we had to retrieved it by using their measurements, done one the same sample, at $\lambda = 730nm = 1.7eV$ ($R = 0.114$ and $T = 0.016$). This wavelength corresponds to the d-d band whose absorption coefficient has been previously reported to lay between 200 and 600 cm^{-1} (depending on the source [4, 10]). Therefore, we can retrieve L_{sample} that has been used by Damascelli et al. (195 μm to 65 μm) and then estimate $\alpha_{9\mu m}$: between 5.6 cm^{-1} and 16.9 cm^{-1}. This last values permit to get ΔQ_{pump} and finally to estimate a range of pump-induced temperature increase δT: between 0.94 K and 1.66 K for an initial temperature of 8 K and between 4 mK and 7.3 mK for an initial temperature of 300 K.
According to this estimation, the temperature increase, linked to a complete transfer into heat of the absorbed pump energy, is about 2 orders of magnitude higher at 8 K than the one at 300 K. Nevertheless, we have observed that the transmissivity maps at these two sample temperatures are very similar: we only observe a shift of the overall map toward lower energy (see Supplementary Fig.4). In particular, this shift seems to be linked with the difference in the sample initial temperature which induces a overall shift of the d-d band features toward lower energies of about 60 meV. In other word, the pump-induced thermal effects are certainly negligible or not visible on the probed timescale with respect to the effect of the sample initial temperature. Moreover, the developed model results (see Supplementary Fig.10 for T = 300 K), are also in favor of this interpretation. These theoretical results show that the absorption spectral distribution variations (central energy and the energy bandwidth shifts) which are induced by a $\delta T = 10^{-2}$ K at 300 K (resp. a $\delta T = 1$ K at 8 K) are negligible with respect to the ones induced by a relevant displacement variation (ΔB_t) in the same conditions.

2.2 Pump wavelength dependency

In order to obtain a better insight on the role of the pump in the probed dynamics, we have performed some preliminary transmissivity measurements along the c-axis and the b-axis of $CuGeO_3$, at 300 K, as a function of the pump wavelength and for two given probe photon energies (Supp. Fig.5). Besides, in the current subsection, the data are issued from an anterior set of measurements for which the pump duration and the probe duration were longer: it justifies the mismatches comparing to the data that are shown in the main text (Fig.2(b)).

Pump wavelength dependence at $\mathbf{E}_{probe} = 1.7$, c-axis vs b-axis (Supplementary Fig.5.(a)-(b)). Compared to the c-axis (main text Fig.2(a)), the b-axis does not show a quick variation of ΔT/T around delay zero but only long timescale population dynamics are observed. These slow population dynamics are especially intense for two pump wavelengths around 9 μm and 11 μm. Such as for the c-axis, these long timescale dynamics appear for pump wavelengths which correspond to reasonable dips in the optical transmission (displayed in the right panels of Supplementary Fig.5.(a)-(b)), that are around 9 μm and 10.7 μm for the b-axis. Besides, for both axis, some measurements have been performed for pump wavelength from 13 μm to 17 μm, but nothing clear was observed (very

noisy signals). This is is notably justified by the fact that the midIR light cannot propagate inside the media at these wavelengths (see 2.2).

Pump wavelength dependence at $\mathbf{E}_{probe} = 1.37$, c-axis vs b-axis (Supplementary Fig.5.(c)-(d)). We also wanted to understand better the role of the pump concerning the transient transparency that has been observed in the low-energy range (below 1.45 eV), namely out of the d-d transitions. Therefore, we have performed a set of pump wavelength dependent measurements keeping the probe photon energy at 1.37 eV and the results are shown in Supp. Fig.5.e-h. We can clearly observe that, on the c-axis, the maximum of this transient transparency is around $\lambda_{pump} \approx 9\mu$m whereas on the b-axis a maximum of this transparency appears around $\lambda_{pump} \approx 8\mu$m. The c-axis map clearly confirms that the maximum amplitude of the coherent effects is obtained for $\lambda_{pump} = 8\mu$m which is located out of the phonon modes.

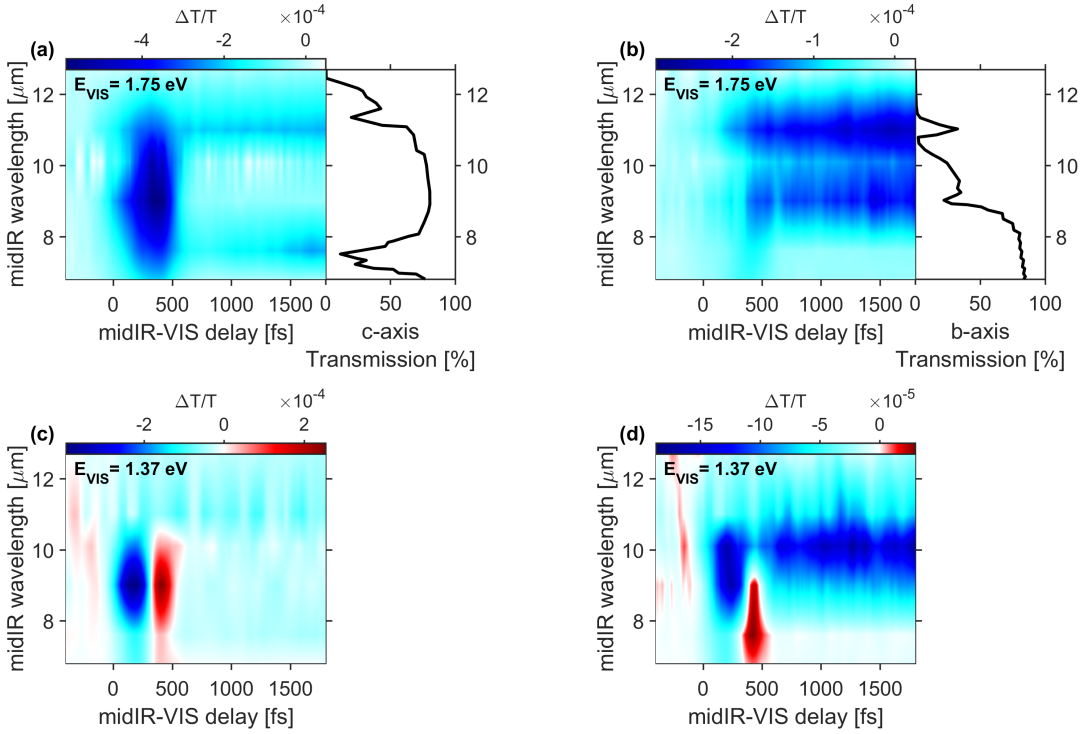

Figure 5: (a-b): Comparison of the pump-wavelength dependence transmissivity maps for (a) the c-axis and (b) the b-axis in the case of $E_{probe} = 1.7eV$. For each crystallographic axis, the optical transmission has been plotted on the same energy range on the right panel (reproduced from [2]. (c-d) Comparison of pump-wavelength dependence transmissivity maps for the c-axis and the b-axis in the case of $E_{probe} = 1.37eV$.

Finite difference time domain (FDTD) simulation of electromagnetic wave propagation The lattice polarization (P(x,t)) induced by the pump pulse has been computed using a finite-difference time-domain (FDTD) code [11, 12]. First, we have calculated the maximum polarization amplitude that develops inside the material as a function of pump wavelength. The optical properties of $CuGeO_3$ have been retrieved by fitting the measured reflectivity. Typically, this maximum is reached at the sample surface and at time zero, i.e. when the pulse hits the material. The result of this calculation is displayed in Supp. Fig.6 for a pump pulse duration of 200 fs (green curve).

As expected the maximum value is reached for photon energies within the *reststrahlen* band(s), i.e. around 750 cm^{-1} ($\approx 13.5\mu$m) and 530 cm^{-1} ($\approx 19\mu$m), which is where the screening is more efficient. Secondly, we have estimated the effects of penetration dept mismatch between the pump and the probe in a transmission experiment. While the probe is transmitted by the material, thus probing the entire sample thickness, the pump penetration depth strongly depends on the frequency. In the *reststrahlen* band, the pump excites, albeit with maximum intensity, only few hundreds of nanometers. On the other hand, for pump frequencies higher than the *reststrahlen* band, the coupling to the phonon is still sizeable while the penetration depth grows (hundreds of microns). As a result, the overall effect seen by the probe is maximized in this spectral region. In first approximation, for each pump wavelength this effect can be estimated by first integrating the polarization in space for a given pump-probe delay and then by taking the maximum value of the resulting vector. The maximum of the integrated polarization estimates the effect of the pump-probe penetration depth mismatch and is depicted in Supp. Fig.6 (red curve) as a function of pump wavelength. We can clearly observe that the integrated polarization peaks around 900 cm^{-1} ($\approx 11\mu$m), on the right side of the *reststrahlen* band. This value is not so far from the one that was used during the experiment (9 μm). Many factors could be considered to get results that are more realistic: (i) by integrating the polarization in space for a given pump-probe delay, we assume the probe group velocity to be infinite, therefore neglecting the probe dispersion, (ii) The simulated phononic response to the pump field is considered to be linear. However, pump-activated non-linearities could reshape the phononic spectrum thus affecting the dynamics. (iii) Our simulations only consider infrared-active single-phonon resonances. Multiple-phonon resonances or impurity centers also appear in the mid-infrared optical properties, albeit with smaller oscillator strengths.

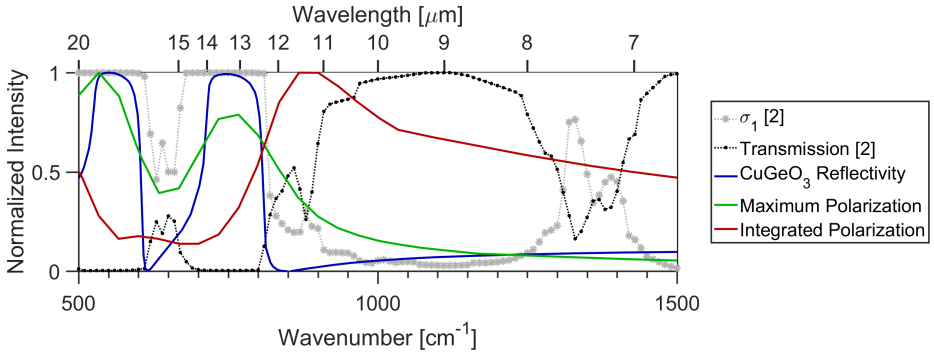

Figure 6: Computed polarization vector maximum for $CuGeO_3$ (blue curve is the reflectivity) at the surface (green) or taking into account the propagation effect inside (red) compared to the experimental optical conductivity σ_1 (gray circle) or transmission (black dot); data reproduced from [2].

The blue shift of the effect observed in our simulations is compatible with the measurements shown in Supplementary Fig.5, where higher coherent effects are detected for pump wavelengths blueshifted with respect to the targeted phonon mode. Overall, our measurements demonstrate the presence of a coherent response associated to mid-IR excitation which appears to be resonant at 9μm and is well described by the phonon assisted dd-transition gated by a coherent vibrational states involving the octaherdral ions. The mechanism for generating such a coherent motion of the ions is compatible with phonon non-linearities but the presence of a mid-IR resonance at 9μm invisible to linear response cannot be excluded and will be the subject of further studies.

2.3 Phonon mode on long timescale

The zoom in the transmissivity map at 8 K shows an additional feature on long timescale: a phonon mode is excited (see Supplementary Fig.7 for 8K). The extracted frequency is about 182 cm^{-1} which is thus associated to the A_g phonon mode at 187 cm^{-1} [3]. This demonstrates the possibility to excite Raman modes through anharmonic couplings on long timescale.

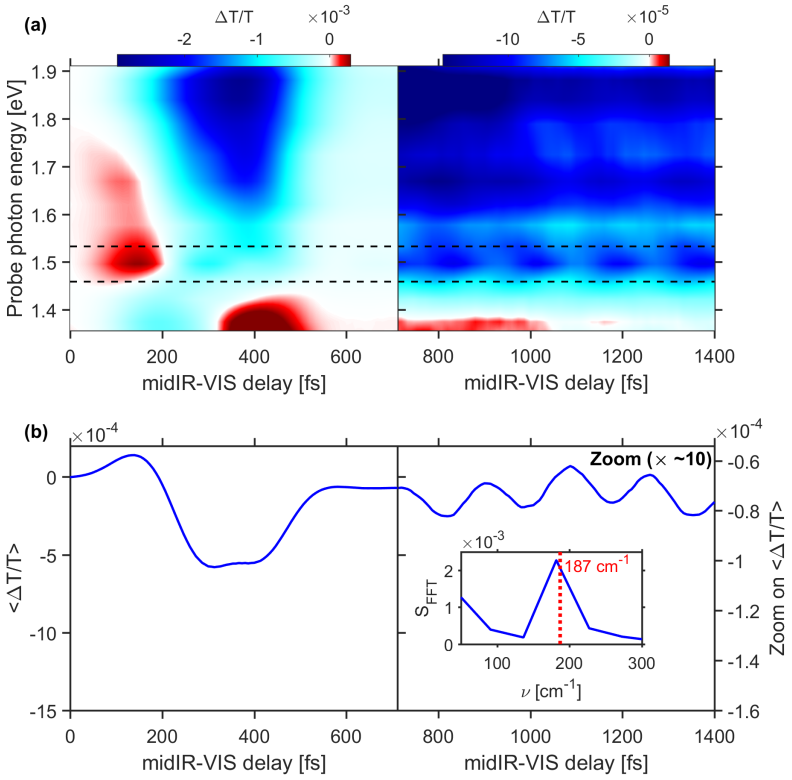

Figure 7: (a) Right part: zoom in transmissivity map at 8 K, the color scale has been divided by 20. (b) Right part: zoom on $< \Delta T/T >$ that has been averaged between 1.46 and 1.53 eV (dashed lines on (a)). The inner panel shows the Fourier transform of the right panel signal and the red dashed line corresponds to the lowest A_g phonon mode at 187 cm^{-1}.

3 Theory

In the following, we discuss the details of the theoretical model used in the main text. A localized d-d transition is described by means of a two-level system interacting with a single vibrational mode of the crystal represented by a quantum harmonic oscillator. As discussed in the main text, our theoretical model assumes the electronic transitions to be induced by the interaction of the sample electronic and phononic degrees of freedom with the probe light. The probe light is first described as a classical field in Section 3.2 while in Section 3.3 we adopt a fully quantum picture. In this latter context, by choosing a dipolar electron-phonon-photon interaction we can compute the average number of transmitted photons at a certain frequency, up to leading order in perturbation theory. This in turn gives information about the absorption spectrum of the sample in the frequency range pertaining to the electronic degrees of freedom, which, for sake of simplicity, have been restricted to a single dressed electronic transition. The theoretical expressions for the relevant quantities are derived firstly by considering the sample in thermal phononic equilibrium and afterwards by taking into account the phonon displacement induced by the pump pulse. The expected temperature dependence of the absorption profile, consistent with the experimental findings [4], is correctly predicted by our model. An overall enhancement of the integrated absorption is predicted as well, together with a shift of the average frequency of the transmitted photon distribution. Finally, in Section 3.4 a justification of the dipolar three-body interaction is given in terms of the standard theoretical treatment of molecular spectroscopy which is well suited for this kind of localized transitions. Summarizing, our theoretical model allows us to generalize the Fermi Golden Rule to the case of states that are not diagonal (have quantum coherence) in the sample energy eigenbasis. Moreover, it is consistent with previously known results, inasmuch it predicts the correct temperature dependence of the frequency integrated absorption. More remarkably, it predicts the shift of the absorption profile due to the pump-induced displacement of atoms in the lattice, that in turn causes transient transparency in some frequency ranges as detected by our experiment.

3.1 Phonon-dressed d-d transition

In absence of probe light, the dynamics of the relevant electronic and phononic degrees of freedom is described through the following model Hamiltonian:

$$H_{ph-el} \equiv H = \omega\, b^\dagger b + \epsilon\, d^\dagger d + M d^\dagger d\,(b + b^\dagger), \tag{3}$$

where $b, b^\dagger$ are bosonic operators describing the vibrational degree of freedom modulating the electronic transitions, with the electronic degrees of freedom described by the fermionic operators $d, d^\dagger$. The parameters ω and ϵ represent the bare phonon frequency and electronic transition energy, respectively, while M is the coupling between the two degrees of freedom.
This model Hamiltonian can be explicitly diagonalized [13]. Indeed, one can find a diagonal Hamiltonian $\widetilde{H}$

$$\widetilde{H} = \omega\, b^\dagger b + \left(\epsilon - \frac{M^2}{\omega}\right) d^\dagger d \tag{4}$$

that is related to H by a unitary transformation U

$$\widetilde{H} = U^\dagger\, H\, U, \quad U = \mathrm{e}^{-\frac{M}{\omega} d^\dagger d (b^\dagger - b)}. \tag{5}$$

As a consequence, the eigenvalues of $\widetilde{H}$ correspond to the eigenvalues of H

$$sp(H) = \left\{ n\omega \,\middle|\, n \in \mathbb{N} \right\} \cup \left\{ n\omega + \epsilon - \frac{M^2}{\omega} \,\middle|\, n \in \mathbb{N} \right\}, \tag{6}$$

while the eigenvectors $|\psi\rangle_n^m$ of H are obtained from the eigenvectors $|\widetilde{\psi}\rangle_n^m$ of $\widetilde{H}$ through the unitary operator U

$$|\psi\rangle_n^m = U|\widetilde{\psi}\rangle_n^m, \quad |\widetilde{\psi}\rangle_n^m = |n\rangle \otimes |m\rangle = \frac{(b^\dagger)^n}{\sqrt{n!}}|0\rangle \otimes (d^\dagger)^m|0\rangle, \tag{7}$$

with $n \in \mathbb{N}$ and $m \in \{0, 1\}$. More explicitly, the action of U has no effect on the eigenstates $|\widetilde{\psi}\rangle_n^0$ corresponding to the electronic ground state, namely $|\psi\rangle_n^0 = |\widetilde{\psi}\rangle_n^0$, while the phonon eigenstates describing the electronic excited state are displaced proportionally to the coupling constant M

$$|\psi\rangle_n^1 = \mathrm{e}^{-\frac{M}{\omega}(b^\dagger - b)}|n\rangle \otimes |1\rangle. \tag{8}$$

Therefore, the Hamiltonian H accounts for a potential energy surface corresponding to the electronic excited state whose minimum is shifted with respect to the ground state. This fact can be easily recognized comparing the average phonon position quadrature $b + b^\dagger$ in the two states $|\psi\rangle_0^1$ and $|\psi\rangle_0^0$ (electron in the excited or ground state respectively and no vibrational excitation)

$${}_0^0\langle\psi|(b + b^\dagger)|\psi\rangle_0^0 = 0, \quad {}_0^1\langle\psi|(b + b^\dagger)|\psi\rangle_0^1 = -2\frac{M}{\omega}. \tag{9}$$

3.2 Probe-target interaction (phonon thermal equilibrium)

In the pump-probe setup of our experiment two different light pulses interact with the sample. An infrared pump pulse induces coherent vibrations in the crystal (along a specific normal mode) and after a delay-time t a visible probe pulse induces electronic transitions.
Let us concentrate for the moment on the interaction between the probe light and the electron-phonon system. We assume the sample system to be in the electronic ground state with a thermal distribution of the relevant vibrational excitation. Using the notation introduced in the previous section, the initial state for the electron-phonon system at a given inverse temperature β reads

$$\varrho = \varrho_\beta \otimes |0\rangle\langle 0|, \quad \varrho_\beta = \frac{\mathrm{e}^{-\beta\omega n}}{\mathrm{Tr}(\mathrm{e}^{-\beta\omega b^\dagger b})}|n\rangle\langle n|. \tag{10}$$

Notice that, since $d^\dagger d|0\rangle = 0$, such a state ϱ is invariant under the time-evolution generated by H in (3). The electronic transitions are therefore induced by the interaction with the probe light that we describe in this section as a classical electric field $E(t) = \sum_k(\alpha_k \mathrm{e}^{i\nu_k t} + \alpha_k^* \mathrm{e}^{-i\nu_k t})$, so that we have an effective time-dependent Hamiltonian for the evolution of the phonon-electron system

$$\widetilde{H}_{int} = \mu_0 E(t) P, \quad P = (b + b^\dagger)(d + d^\dagger), \tag{11}$$

where the operator P is a dipole moment operator for the sample. In general, the term $d + d^\dagger$ has to be expected because it gives transitions from the electronic ground state to the electronic excited state while the further term $b + b^\dagger$ describes how the phonon position quadrature influences the electronic transitions. This choice for the dipole operator will be justified in Section 3.4 by means of molecular physics arguments. Given the perturbation $\widetilde{H}_{int}$, standard considerations of atomic/molecular spectroscopy [14] and the Fermi Golden Rule yield an absorption spectrum of the form

$$A(\nu) = \sum_\ell \Gamma_\ell \, \delta(\nu - \epsilon + M^2/\omega - \omega\ell), \tag{12}$$

where the quantities Γ_ℓ are related to the transition probability rates induced by the electronic dipole moment operator P from the electronic ground state to the electronic excited state, producing ℓ

phonons. In particular, considering a thermal phononic initial state (10) one has for Γ_ℓ the following expression

$$\Gamma_\ell = \sum_n \frac{\mathrm{e}^{-\beta\omega n}}{Z_\beta} |\langle n+\ell| \otimes \langle 1| \mathrm{e}^{\frac{M}{\omega}(b^\dagger - b)} P |n\rangle \otimes |0\rangle|^2. \tag{13}$$

In the case of a phonon-electron Hamiltonian entirely dependent on the phonon population, there would be no unitary operator $U = \exp(\frac{M}{\omega}(b^\dagger - b))$ in (13) and the absorption would be the same as in absence of electron-phonon coupling ($M = 0$). Note that the Fermi Golden Rule could be used because the electronic transitions considered are between eigenstates of the Hamiltonian H for the initial electron-phonon state that is diagonal in the eigenbasis of H. A theoretical model will be presented in the next section to account for the case of a non diagonal state. Such a model is based on a change in perspective: the probe light will be no longer treated as an external classical field but as a collection of quantum degrees of freedom. The model we will introduce allows to study the backaction of the sample on the probe light (that is the quantity actually measured in the experiment), so that we can extend the perturbative treatment to more general initial states.
Instead, with an energy diagonal initial state, using the previously defined model, the overall absorption coefficient at finite temperature reads

$$\begin{aligned}\Gamma &= \int \mathrm{d}\nu A(\nu) = |\alpha|^2 \mu_0^2 \sum_m \sum_n \frac{\mathrm{e}^{-\beta\omega n}}{Z_\beta} |\langle m| \mathrm{e}^{\frac{M}{\omega}(b^\dagger - b)} (b + b^\dagger) |n\rangle|^2 \\ &= |\alpha|^2 \mu_0^2 \mathrm{Tr}\left[\varrho_\beta (2b^\dagger b + 1)\right] = \alpha^2 \mu_0^2 \coth\left(\frac{\beta\omega}{2}\right). \end{aligned} \tag{14}$$

where $|\alpha|^2$ is proportional to the intensity of the electromagnetic field. For simplicity, we use $|\alpha|^2 = 1$ in what follows. The expression of Γ is in agreement with experimental findings [4, 10] and previous theoretical studies [15]. Notice that, if $b + b^\dagger$ is replaced by a mean field scalar quantity, then the temperature dependence disappears and this is a clear indication that it is the phonon displacement that really maters, rather the phonon population. The computation of the single absorption lines is a bit more involved. Explicitly, the quantity to be determined is the amplitude of the absorption line corresponding to the transition energy $\Delta E(\ell) = \epsilon - \frac{M^2}{\omega} + \omega\ell$, namely

$$\Gamma_\ell = \mu_0^2 \sum_n \frac{\mathrm{e}^{-\beta\omega n}}{Z_\beta} |\langle n+\ell| \mathrm{e}^{\frac{M}{\omega}(b^\dagger - b)} (b + b^\dagger) |n\rangle|^2. \tag{15}$$

The first step is the computation of the matrix element $\langle m| \mathrm{e}^{\frac{M}{\omega}(b^\dagger - b)} |n\rangle$. Using the following algebraic property

$$\mathrm{e}^{\frac{M}{\omega}(b^\dagger - b)} = \mathrm{e}^{\frac{M}{\omega} b^\dagger} \mathrm{e}^{-\frac{M}{\omega} b} \mathrm{e}^{-\frac{M^2}{2\omega^2}}, \tag{16}$$

one can rewrite the matrix element in a convenient way (for $n \geq m$)

$$\begin{aligned}\langle m| \mathrm{e}^{\frac{M}{\omega}(b^\dagger - b)} |n\rangle &= \mathrm{e}^{-\frac{M^2}{2\omega^2}} \sum_{j=0}^{m} \sum_{i=0}^{n} (-1)^i \left(\frac{M}{\omega}\right)^{i+j} \frac{1}{i!j!} \frac{\sqrt{n!m!}}{\sqrt{(n-i)!(m-j)!}} \langle m-j | n-i\rangle \\ &= \mathrm{e}^{-\frac{M^2}{2\omega^2}} \sum_{j=0}^{m} (-1)^{n-m+j} \left(\frac{M}{\omega}\right)^{n-m+2j} \frac{\sqrt{n!\,m!}}{(n-m+j)!\,j!\,(m-j)!} = \\ &= \mathrm{e}^{-\frac{M^2}{2\omega^2}} (-1)^{n-m} \left(\frac{M}{\omega}\right)^{n-m} \frac{\sqrt{m!}}{\sqrt{n!}} L_m^{n-m}\left(\frac{M^2}{\omega^2}\right), \end{aligned} \tag{17}$$

where the generalized Laguerre polynomials $L_i^j(x)$ are defined as follows [16]

$$L_i^j(x) = \sum_{t=0}^{i} \frac{(-1)^t}{t!} x^t \frac{(i+j)!}{(j+t)!\,(i-t)!}. \tag{18}$$

Also, for $n \leq m$ one can use $\langle m|X|n\rangle = (\langle n|X^\dagger|m\rangle)^*$ and arrive at

$$\langle m|\mathrm{e}^{\frac{M}{\omega}(b^\dagger - b)}|n\rangle = \mathrm{e}^{-\frac{M^2}{2\omega^2}} \left(\frac{M}{\omega}\right)^{m-n} \frac{\sqrt{n!}}{\sqrt{m!}} L_n^{m-n}\left(\frac{M^2}{\omega^2}\right). \tag{19}$$

Coming back to equation (15) one can see that the action of $b^\dagger + b$ gives two matrix elements of the kind discussed before, namely

$$\sqrt{n}\,\langle n+\ell|\mathrm{e}^{\frac{M}{\omega}(b^\dagger - b)}|n-1\rangle + \sqrt{n+1}\,\langle n+\ell|\mathrm{e}^{\frac{M}{\omega}(b^\dagger - b)}|n+1\rangle, \tag{20}$$

that in turn can be rewritten using (19) (assume $\ell \geq 1$ for now)

$$\begin{aligned}
&\mathrm{e}^{-\frac{M^2}{2\omega^2}} \left[\left(\frac{M}{\omega}\right)^{\ell+1} \frac{\sqrt{n!}}{\sqrt{(n+\ell)!}} L_{n-1}^{\ell+1}\left(\frac{M^2}{\omega^2}\right) + (n+1)\left(\frac{M}{\omega}\right)^{\ell-1} \frac{\sqrt{n!}}{\sqrt{(n+\ell)!}} L_{n+1}^{\ell-1}\left(\frac{M^2}{\omega^2}\right)\right] = \\
&= \mathrm{e}^{-\frac{M^2}{2\omega^2}} \left(\frac{M}{\omega}\right)^{\ell-1} \frac{\sqrt{n!}}{\sqrt{(n+\ell)!}} \left[\frac{M^2}{\omega^2} L_{n-1}^{\ell+1}\left(\frac{M^2}{\omega^2}\right) + (n+1) L_{n+1}^{\ell-1}\left(\frac{M^2}{\omega^2}\right)\right].
\end{aligned} \tag{21}$$

One can now exploit the recurrence relation of Laguerre polynomials [16]

$$(n+1)L_{n+1}^{\ell-1}(x) + xL_{n-1}^{\ell+1}(x) = (\ell - x)L_n^\ell(x), \tag{22}$$

and arrive at

$$\langle n+\ell|\mathrm{e}^{\frac{M}{\omega}(b^\dagger - b)}(b + b^\dagger)|n\rangle = \mathrm{e}^{-\frac{M^2}{2\omega^2}} \left(\frac{M}{\omega}\right)^{\ell-1} \frac{\sqrt{n!}}{\sqrt{(n+\ell)!}} \left(\ell - \frac{M^2}{\omega^2}\right) L_n^\ell\left(\frac{M^2}{\omega^2}\right). \tag{23}$$

Therefore, it remains to compute the quantity

$$\Gamma_\ell = \mu_0^2 \sum_{n=0}^{\infty} \frac{\mathrm{e}^{-\beta\omega n}}{Z_\beta} \mathrm{e}^{-\frac{M^2}{\omega^2}} \left(\frac{M^2}{\omega^2}\right)^{\ell-1} \frac{n!}{(n+\ell)!} \left(\ell - \frac{M^2}{\omega^2}\right)^2 \left(L_n^\ell\left(\frac{M^2}{\omega^2}\right)\right)^2. \tag{24}$$

This can be done by means of the so-called Hardy-Hille formula [16]

$$\sum_{n=0}^{\infty} \frac{n!}{(n+\ell)!} t^n L_n^\ell(x) L_n^\ell(y) = \frac{\mathrm{e}^{-\frac{(x+y)t}{1-t}}}{(xyt)^{\ell/2}(1-t)} I_\ell\left(\frac{2\sqrt{xyt}}{1-t}\right), \tag{25}$$

where $I_\ell(x)$ is a modified Bessel function of the first kind. The final expression reads

$$\Gamma_\ell = \mu_0^2 \frac{\omega^2}{M^2} \left(\ell - \frac{M^2}{\omega^2}\right)^2 \mathrm{e}^{\beta\omega\ell/2} \mathrm{e}^{-\frac{M^2}{\omega^2}\coth(\beta\omega/2)} I_\ell\left(\frac{M^2}{\omega^2 \sinh(\beta\omega/2)}\right). \tag{26}$$

A similar treatment can be used to study the case $\ell < 1$ and it turns out that the expression (26) is true for any ℓ, using the property $I_{-\ell} = I_\ell$. Some information can be extracted by looking at the asymptotic behavior of the modified Bessel function for small or large argument

$$I_\ell(x) \simeq \frac{1}{\ell!}\left(\frac{x}{2}\right)^\ell, \qquad 0 < x \ll \sqrt{\ell+1}. \tag{27}$$

In particular, when the phonon-electron coupling is small $M \to 0$, so that one can use the relation (27), it turns out that

$$\Gamma_\ell \simeq \mu_0^2 \ell^2 \frac{\mathrm{e}^{\beta\omega\ell/2}}{|\ell|!} \frac{1}{2\sinh^{|\ell|}(\beta\omega/2)} \left(\frac{M^2}{2\omega^2}\right)^{|\ell|-1} \qquad \ell \neq 0, \tag{28}$$

$$\Gamma_0 \simeq \mu_0^2 \frac{M^2}{\omega^2}. \tag{29}$$

As a consequence, for vanishing coupling M only the absorption lines with $\ell = 1$ or $\ell = -1$ are non-zero and the line with $\ell = -1$ is $\mathrm{e}^{-\beta\omega}$ smaller than the other. In the zero-temperature limit $\beta \to \infty$ only the latter survives (the system is initially in the ground state and cannot lower the number of phonons).

3.3 Probe-target interaction (general case)

In the general case, when the initial state is not diagonal in the electron-phonon energy eigenbasis because it has been modified by the pump pulse, the Fermi Golden Rule cannot be applied. Therefore, we use here a more general treatment where the probe light is considered explicitly as a quantum field and it is measured after the interaction with the sample. The interaction between the probe light pulse and the excited sample is described trough the following interaction Hamiltonian

$$H_{int} = \mu_0 P \sum_k (a_k^\dagger + a_k), \quad P = (b + b^\dagger)(d + d^\dagger), \tag{30}$$

where the annihilation and creation operators a_k and $a_k^\dagger$ are related to the light mode of frequency ν_k. Because of the perturbative character of the interaction Hamiltonian H_{int}, the evolution of the mean photon number $a_j^\dagger a_j$ relative to the mode ν_j in a time-interval τ can be computed by a second order truncation of the Dyson series

$$\mathrm{Tr}\Big(\varrho\, U^\dagger(\tau) a_j^\dagger a_j U(\tau)\Big) \simeq \tag{31}$$

$$\mathrm{Tr}\left(\varrho\left(a_j^\dagger a_j + i\lambda \int_0^\tau \Big[H_{int}(s), a_j^\dagger a_j\Big] \mathrm{d}s - \lambda^2 \int_0^\tau \mathrm{d}s \int_0^s \mathrm{d}u \Big[H_{int}(u), \Big[H_{int}(s), a_j^\dagger a_j\Big]\Big]\right)\right). \tag{32}$$

The first term $\mathrm{Tr}\left(\varrho\, a_j^\dagger a_j\right)$ is the unperturbed light intensity corresponding to $|\alpha_j|^2$, by choosing the initial phonon-electron-photon state in the form:

$$\varrho = \overline{\varrho} \otimes |\alpha\rangle\langle\alpha|, \quad \overline{\varrho} = \sum_\ell p_\ell^0 \, |\ell, 0\rangle\langle\ell, 0|, \tag{33}$$

where $|\alpha\rangle$ is a multi-photon coherent state, describing the probe pulse, $a_j|\alpha\rangle = \alpha_j|\alpha\rangle$. One gets a vanishing first order contribution, so that a second order calculation is needed. The above choice of an initial state diagonal in the energy basis provided by the Hamiltonian H (3) is made here to compare this approach to the previous one. More general non diagonal displaced thermal states will be considered later on. The second order term $\Gamma^{(2)}$ reads

$$\Gamma^{(2)} = \mu_0^2 \Big(8i \sum_k \alpha_j \alpha_k \int_0^\tau \mathrm{d}s \int_0^s \mathrm{d}u \, \mathrm{Tr}(\overline{\varrho}[P(s), P(u)]) \sin(s\nu_j) \cos(u\nu_k)\Big) \tag{34}$$

$$+ \mu_0^2 \mathrm{Tr}\big(\overline{\varrho}\, P(s)\, P(u)\big) \mathrm{e}^{i(s-u)\nu_j} + c.c. \tag{35}$$

The term in the second line is due to the bosonic commutation relations of the quantized field and is negligible with respect to the other one for intense light pulses $|\alpha_k| \gg 1$ and for any mode in the considered frequency range. Moreover, in order to avoid complications due to the spectral structure of the incident probe light, we consider from now on the simplifying assumption that α_k be constant for any k in a relevant frequency range. The quantity in the trace can then be easily evaluated

$$\mathrm{Tr}\big(\overline{\varrho}\, P(s)\, P(u)\big) = \sum_{\ell m} p_\ell^0\, \mathrm{e}^{-i(E_m^1 - E_\ell^0)(s-u)} \Big|\langle \ell, 0|P|m, 1\rangle\Big|^2. \tag{36}$$

As a result, the time dependence is given by the following integral

$$\begin{aligned} &8i \int_0^\tau \mathrm{d}s \int_0^s \mathrm{d}u\, (-2i) \sin\big((E_m^1 - E_\ell^0)(s-u)\big) \sin(s\nu_j) \cos(u\nu_k) = \\ &= 4 \left(\frac{1}{\nu_k - \Delta_{m\ell}} - \frac{1}{\nu_k + \Delta_{m\ell}} \right) \times \\ &\times 2 \left(\frac{\sin^2\left(\tau \frac{\nu_j + \nu_k}{2}\right)}{\nu_j + \nu_k} + \frac{\sin^2\left(\tau \frac{\nu_j - \nu_k}{2}\right)}{\nu_j - \nu_k} - \frac{\sin^2\left(\tau \frac{\nu_j + \Delta_{m\ell}}{2}\right)}{\nu_j + \Delta_{m\ell}} - \frac{\sin^2\left(\tau \frac{\nu_j - \Delta_{m\ell}}{2}\right)}{\nu_j - \Delta_{m\ell}} \right) \end{aligned} \tag{37}$$

with $\Delta_{m\ell} = E_m^1 - E_\ell^0$. By defining the function $D_\tau(x) = \frac{4\sin^2(\tau x/2)}{x^2}$ we see that the function $\delta_\tau(x) = \frac{1}{2\pi\tau} D_\tau(x)$ is a representation of the Dirac delta in the limit $\tau \to \infty$. Therefore, one finds for the rate of change in transmissivity at frequency ν_j

$$\lim_{\tau\to\infty} \frac{\Gamma^{(2)}(\tau)}{\tau} = -4\pi\mu_0^2 \sum_{\ell m} p_\ell^0 \Big|\langle \ell, 0|P|m, 1\rangle\Big|^2 \delta(\nu_j - \Delta_{m\ell}) \tag{38}$$

This corresponds to the rate computed through the Fermi golden rule with a minus sign.
We now perform the same calculation for a state $\overline{\varrho}$ of the form

$$\overline{\varrho} = \sum_\ell p_\ell^0\, D|\ell, 0\rangle\langle \ell, 0|D^\dagger, \tag{39}$$

where $D = \mathrm{e}^{B_t(b^\dagger - b)}$ is a phononic displacement operator sending b into $b - B_t$, with B_t a time modulated real parameter. The case we are particularly interested in is when the operator $\overline{\varrho}$ is obtained acting with the displacement operator on the thermal state, namely when $\overline{\varrho} = D\varrho_\beta D^\dagger$. In this case $\overline{\varrho}$ is a so-called displaced thermal state, that accounts for large fluctuations of the position quadrature at high temperature, and at the same time yields a nonzero average value of the position quadrature depending on the amount of phononic displacement (quantified by the parameter B_t). This kind of description is used in the following in order to account for the excitation of the vibrational degree of freedom in the sample due to the infrared pump pulse. Indeed, in the following, we model the dynamics induced by the pump as a time-dependent displacement operator acting on the vibrational degree of freedom. This is a realistic scenario when describing, for instance, stimulated Raman scattering [17]. In what follows, the effects of the interaction of the sample with the pump are implicitly encoded in the external phonon displacing parameter B_t, without dynamically predicting its functional form.
The absorption rate can be calculated as before, but now the correlation function $\mathrm{Tr}\big(\overline{\varrho}\, P(s)\, P(u)\big)$ reads

$$\begin{aligned} \mathrm{Tr}\big(\overline{\varrho}\, P(s)\, P(u)\big) = \sum_{\ell m n v} & p_\ell^0 \langle \ell, 0|D^\dagger|m, 0\rangle\langle m, 0|P|n, 1\rangle\langle n, 1|P|v, 0\rangle\langle v, 0|D|\ell, 0\rangle \times \\ & \times \mathrm{e}^{-is\Delta_{nm}}\, \mathrm{e}^{iu\Delta_{nv}}. \end{aligned} \tag{40}$$

Integrating in time and performing the same limit as before for the rate one finds

$$\lim_{\tau\to\infty}\frac{\Gamma^{(2)}(\tau)}{\tau}=\mu_0^2\delta(\nu_j-\bar{\epsilon}-\omega\ell)\sum_n\langle n|D\varrho_\beta D^\dagger(b+b^\dagger)\mathrm{e}^{-\frac{M}{\omega}(b^\dagger-b)}|n+\ell\rangle\times$$
$$\times\langle n+\ell|\mathrm{e}^{\frac{M}{\omega}(b^\dagger-b)}(b+b^\dagger)|n\rangle+c.c.$$

Therefore, the spectral line Γ_ℓ reads

$$\Gamma_\ell=\mu_0^2\sum_n\langle n|D\varrho_\beta D^\dagger(b+b^\dagger)\mathrm{e}^{-\frac{M}{\omega}(b^\dagger-b)}|n+\ell\rangle\langle n+\ell|\mathrm{e}^{\frac{M}{\omega}(b^\dagger-b)}(b+b^\dagger)|n\rangle. \tag{41}$$

We can first discuss the total absorption as in the equilibrium case. The calculation is quite straightforward as it amounts to summing over all ℓ indexes and the result is

$$\Gamma=\sum_{\ell=-\infty}^{+\infty}\Gamma_\ell=\mu_0^2\left(\coth\left(\frac{\beta\omega}{2}\right)+4B_t^2\right). \tag{42}$$

With respect to the thermal state calculation (14), we see a displacement-dependent offset to the temperature dependence. According to this model, the correction to the total absorption is always positive and again independent of whether the phonon mode ω is electronically active ($M\neq 0$) or not ($M=0$) and of whether the phonon-electron coupling is via the phonon-population. However, it is interesting to see how the spectral weight shifts depending on B_t, because such is the experimental evidence we would like to reproduce. This is done in the following, computing each single absorption term Γ_ℓ. Notice that for, large times, due to dissipative effects resulting from the phonon interacting with other sample degrees of freedom, the vibrational initial state is expected to relax to a thermal state at higher temperature, possibly still displaced but, unlike the initial one subjected to the pump pulse, by a quantity B independent of time. Therefore, unlike the displacement at short times, the one in the long time regime will not give rise to the temporal shift of the absorption lines that are associated with transparency effects.
Let us start with the case $\ell>0$. The first matrix element can be conveniently rewritten exploiting the bosonic commutation relations

$$\begin{aligned}
&\langle n|D\varrho_\beta D^\dagger(b+b^\dagger)\mathrm{e}^{-\frac{M}{\omega}(b^\dagger-b)}|n+\ell\rangle=\\
=&\mu_0^2\frac{\mathrm{e}^{-\beta\omega n}}{Z_\beta}\langle n|\mathrm{e}^{B_t(\mathrm{e}^{\beta\omega}b^\dagger-\mathrm{e}^{-\beta\omega}b)}(b^\dagger+b+2B_t)\mathrm{e}^{-(\frac{M}{\omega}+B_t)(b^\dagger-b)}|n+\ell\rangle=\\
=&\mu_0^2\frac{\mathrm{e}^{-\beta\omega n}}{Z_\beta}\langle n|(b^\dagger+b-2B_t\cosh(\beta\omega)+2B_t)\mathrm{e}^{B_t(\mathrm{e}^{\beta\omega}b^\dagger-\mathrm{e}^{-\beta\omega}b)}\mathrm{e}^{-(\frac{M}{\omega}+B_t)(b^\dagger-b)}|n+\ell\rangle=\\
=&\mu_0^2\frac{\mathrm{e}^{-\beta\omega n}}{Z_\beta}\mathrm{e}^{-B_t(\frac{M}{\omega}+B_t)\sinh(\beta\omega)}\langle n|\left(b+b^\dagger-4B_t\sinh^2\left(\frac{\beta\omega}{2}\right)\right)\mathrm{e}^{b^\dagger x+by}|n+\ell\rangle
\end{aligned} \tag{43}$$

where the coefficients x and y are defined as follows

$$x=-\frac{M}{\omega}+B_t(\mathrm{e}^{\beta\omega}-1),\quad y=\frac{M}{\omega}+B_t(1-\mathrm{e}^{-\beta\omega}). \tag{44}$$

Finally one has

$$\begin{aligned}
&\langle n|D\varrho_\beta D^\dagger(b+b^\dagger)\mathrm{e}^{-\frac{M}{\omega}(b^\dagger-b)}|n+\ell\rangle=\\
=&\mu_0^2\frac{\mathrm{e}^{-\beta\omega n}}{Z_\beta}\mathrm{e}^{-\frac{M^2}{2\omega^2}(1+2\frac{\omega B_t}{M}(1+\frac{\omega B_t}{M})(1-\mathrm{e}^{-\beta\omega}))}\langle n|\left(b+b^\dagger-4B_t\sinh^2\left(\frac{\beta\omega}{2}\right)\right)\mathrm{e}^{xb^\dagger}\mathrm{e}^{yb}|n+\ell\rangle
\end{aligned} \tag{45}$$

Using again the properties of bosonic operators one can write for $m > n$

$$\langle n|\mathrm{e}^{xb^\dagger}\mathrm{e}^{yb}|m\rangle = \frac{\sqrt{n!}}{\sqrt{m!}} y^{m-n} L_n^{m-n}(-xy), \tag{46}$$

where the product $-xy$ explicitly reads

$$-xy = \frac{M^2}{\omega^2} - 4B_t\Big(\frac{M}{\omega} + B_t\Big)\sinh^2\Big(\frac{\beta\omega}{2}\Big). \tag{47}$$

The matrix element $\langle n|\Big(b + b^\dagger - 4B_t\sinh^2\big(\frac{\beta\omega}{2}\big)\Big)\mathrm{e}^{xb^\dagger}\mathrm{e}^{yb}|n+\ell\rangle$ then reads

$$\sqrt{n}\langle n-1|X|n+\ell\rangle + \sqrt{n+1}\langle n+1|X|n+\ell\rangle - 4B_t\sinh^2\Big(\frac{\beta\omega}{2}\Big)\langle n|X|n+\ell\rangle, \tag{48}$$

where $X = \mathrm{e}^{xb^\dagger}\mathrm{e}^{yb}$, and can be rewritten accordingly as

$$\frac{\sqrt{n!}}{\sqrt{(n+\ell)!}}\Big[y^{\ell-1}\Big(y^2 L_{n-1}^{\ell+1}(-xy) + (n+1)L_{n+1}^{\ell-1}(-xy)\Big) - 4B_t\sinh^2\Big(\frac{\beta\omega}{2}\Big)y^\ell L_n^\ell(-xy)\Big]. \tag{49}$$

Using the recurrence relations for the Laguerre polynomials one finds

$$\frac{\sqrt{n!}}{\sqrt{(n+\ell)!}} y^{\ell-1}\Big[\Big((\ell+xy) - 4B_t y\sinh^2\Big(\frac{\beta\omega}{2}\Big)\Big)L_n^\ell(-xy) + (y^2+xy)L_{n-1}^{\ell+1}(-xy)\Big]. \tag{50}$$

The first term can be summed as in the time-independent case. In particular, one finds

$$\sum_{n=0}^{\infty}\frac{n!}{(n+\ell)!}\mathrm{e}^{-\beta\omega n}L_n^\ell\Big(-xy\Big)L_n^\ell\Big(\frac{M^2}{\omega^2}\Big) = \frac{\mathrm{e}^{-(\frac{M^2}{\omega^2}-xy)\frac{1}{\mathrm{e}^{\beta\omega}-1}}}{(1-\mathrm{e}^{-\beta\omega})\mathrm{e}^{-\frac{\beta\omega\ell}{2}}\Big(-xy\frac{M^2}{\omega^2}\Big)^{\frac{\ell}{2}}} I_\ell\left(\frac{\big(-xy\frac{M^2}{\omega^2}\big)^{\frac{1}{2}}}{\sinh(\beta\omega/2)}\right) \tag{51}$$

The other one can be also treated explicitly using the property

$$L_{n-1}^{\ell+1}(z) = -\frac{\mathrm{d}}{\mathrm{d}z}L_n^\ell(z). \tag{52}$$

Indeed one can write

$$\begin{aligned}
&\sum_{n=0}^{\infty}\frac{n!}{(n+\ell)!}t^n L_{n-1}^{\ell+1}(z)L_n^\ell(w) = \\
&= -\frac{\mathrm{d}}{\mathrm{d}z}\sum_{n=0}^{\infty}\frac{n!}{(n+\ell)!}t^n L_n^\ell(z)L_n^\ell(w) = \\
&= \frac{(zwt)^{-\ell/2}}{1-t}\mathrm{e}^{-\frac{(z+w)t}{1-t}}\Big[\frac{t}{1-t}\,I_\ell\left(\frac{2\sqrt{zwt}}{1-t}\right) - \frac{\sqrt{wt}}{\sqrt{z}(1-t)}\,I_{\ell+1}\left(\frac{2\sqrt{zwt}}{1-t}\right)\Big].
\end{aligned} \tag{53}$$

The exchange of derivative and summation is allowed by the uniform convergence of the series in compact sets $|z| < a, |w| < b$. In order to prove uniform converegence it is sufficient to notice that

$$|L_n^\ell(z)| \le L_n^\ell(-a), \quad |z| \le a. \tag{54}$$

Indeed, the quantity $|a_n|$ is bounded as follows

$$|a_n| = \frac{n!}{(n+\ell)!}t^n|L_n^\ell(z)||L_n^\ell(w)| \le \frac{n!}{(n+\ell)!}t^n L_n^\ell(-a)L_n^\ell(-b) \equiv M_n \tag{55}$$

and $\sum_n M_n < \infty$. This proves the uniform convergence according to the Weierstrass criterion. The sum reads explicitly

$$\sum_{n=0}^{\infty} \frac{n!}{(n+\ell)!} t^n L_{n-1}^{\ell+1}\Big(-xy\Big) L_n^{\ell}\Big(\frac{M^2}{\omega^2}\Big) =$$
$$= \frac{\mathrm{e}^{-(\frac{M^2}{\omega^2}-xy)\frac{1}{\mathrm{e}^{\beta\omega}-1}}}{(1-\mathrm{e}^{-\beta\omega})\mathrm{e}^{-\frac{\beta\omega\ell}{2}}\Big(-xy\frac{M^2}{\omega^2}\Big)^{\frac{\ell}{2}}} \left[\frac{1}{\mathrm{e}^{\beta\omega}-1} I_\ell\left(\frac{\big(-xy\frac{M^2}{\omega^2}\big)^{\frac{1}{2}}}{\sinh(\beta\omega/2)}\right) - \frac{\frac{M}{\omega}}{2\sinh(\beta\omega/2)(-xy)^{1/2}} I_{\ell+1}\left(\frac{\big(-xy\frac{M^2}{\omega^2}\big)^{\frac{1}{2}}}{\sinh(\beta\omega/2)}\right)\right] \tag{56}$$

A similar calculation can be performed in the case $\ell \leq 0$:

$$\Gamma_\ell = \mu_0^2(\ell - A)\frac{\mathrm{e}^{-A\coth(C)}\mathrm{e}^{C\ell}}{\Big(1-4\widetilde{B}_t(1+\widetilde{B}_t)\sinh^2(C)\Big)^{\ell/2}}\Big(1+\widetilde{B}_t(1-\mathrm{e}^{-2C})\Big)^{\ell-1} A^{-1}\times$$
$$\times\left[\Big(\ell - A + A\widetilde{B}_t\big(1+\mathrm{e}^{-2C}+2\widetilde{B}_t(1-\mathrm{e}^{-2C})\big)\Big) I_\ell\Big(\frac{A(1-4\widetilde{B}_t(1+\widetilde{B}_t)\sinh^2(C))^{1/2}}{\sinh(C)}\Big) + \right.$$
$$\left. - AB\frac{\sinh(2C)(1+\widetilde{B}_t(1-\mathrm{e}^{-2C}))}{\sinh(C)(1-4\widetilde{B}_t(1+\widetilde{B}_t)\sinh^2(C))^{1/2}} I_{\ell+1}\Big(\frac{A(1-4\widetilde{B}_t(1+\widetilde{B}_t)\sinh^2(C))^{1/2}}{\sinh(C)}\Big)\right], \quad \ell > 0, \tag{57}$$

$$\Gamma_\ell = \mu_0^2(|\ell| + A)\frac{\mathrm{e}^{-A\coth(C)}\mathrm{e}^{C\ell}}{\Big(1-4\widetilde{B}_t(1+\widetilde{B}_t)\sinh^2(C)\Big)^{|\ell|/2}}\Big(1-\widetilde{B}_t(\mathrm{e}^{2C}-1)\Big)^{|\ell|-1} A^{-1}\times$$
$$\times\left[\Big(|\ell| + A - 2A\widetilde{B}_t\big(\frac{\mathrm{e}^{2C}\sinh(2C)}{\mathrm{e}^{2C}-1} - \widetilde{B}_t(\mathrm{e}^{2C}-1)\big)\Big) I_{|\ell|}\Big(\frac{A(1-4\widetilde{B}_t(1+\widetilde{B}_t)\sinh^2(C))^{1/2}}{\sinh(C)}\Big) + \right.$$
$$\left. - A\widetilde{B}_t\frac{-\sinh(2C)+2\widetilde{B}_t\sinh^2(C)(\mathrm{e}^{2C}+1)}{\sinh(C)(1-4\widetilde{B}_t(1+\widetilde{B}_t)\sinh^2(C))^{1/2}} I_{|\ell|+1}\Big(\frac{A(1-4\widetilde{B}_t(1+\widetilde{B}_t)\sinh^2(C))^{1/2}}{\sinh(C)}\Big)\right], \quad \ell \leq 0, \tag{58}$$

where we defined the three adimensional parameters $A, \widetilde{B}_t, C$ as

$$A = \frac{M^2}{\omega^2}, \quad \widetilde{B}_t = B_t\frac{\omega}{M}, \quad C = \frac{\beta\omega}{2}. \tag{59}$$

These three parameters completely specify the model in the approximation we used. The parameter A quantifies the phonon-electron coupling and therefore the displacement of the nuclear positions in the electronic excited state. The parameter $\widetilde{B}_t$ instead is a dynamical one, originated by the pump pulse, and given by the ratio between the light-induced instantaneous displacement and the one due to the electron-phonon coupling, only. Finally, the third parameter, C, specifies the temperature in units of the phonon frequency. In the Supplementary Figure 8.a-c the distributions of the Γ_ℓ are plotted for different values of the parameters A, $\widetilde{B}_t$, and C keeping, for each subfigure, two parameters constant and varying the third one. In particular, we have assumed that: (i) the relevant phonon mode to have a frequency $\omega = 16$ meV, (ii) the coupling constant to be $M = \omega$ in order to match the width of the experimental outcome and (iii) the temperature to be $T = 300$ K ($C = 0.31$) for Supplementary Fig.8.a-b. One can also numerically compute the central energy ($< E >$) and the energy bandwidth

(σ_E) of these distributions. In this respect, Figure 8.a shows that a stronger e-p couplings increases the number of possible transitions, which broadens the distribution, and pushes it toward higher energy. Figure 8.b shows that a higher B_t mostly displaces the overall distribution toward higher energy. Figure 8.c shows that a lower temperature mostly narrows the distribution.

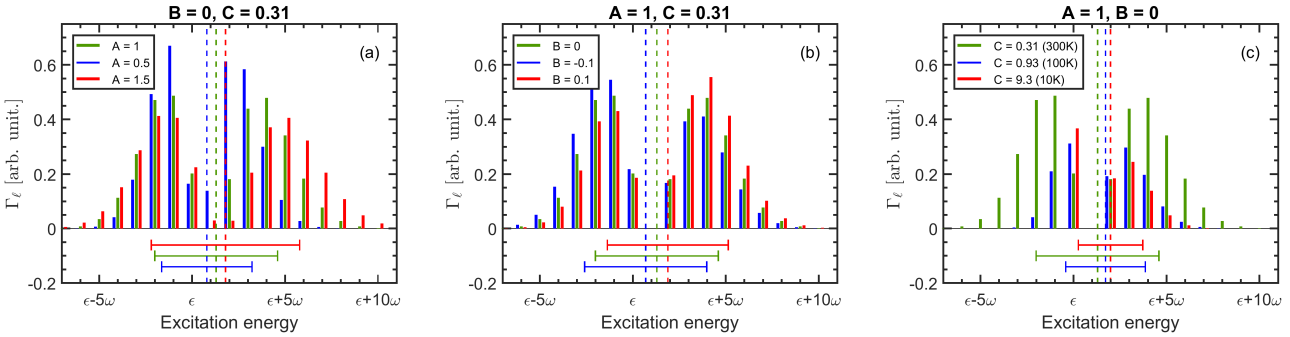

Figure 8: Absorption probability distributions (eq.57-58) for a variation of the three parameters (eq.59): (a) A (strength of the e-p couplings), (b) B (amplitude of the displacement) and (c) C (temperature). For each graph, the values of the two other parameters are kept constant and indicated on the top of the graph. Moreover the central energy (resp. the energy bandwidth) is represented by a vertical dashed line (resp. a horizontal line below the graph).

Then, we can also study the behaviors of the central energy and the energy bandwidth of the distribution as functions of a wide range of temperatures and displacements, in the case $M = \omega = 16$ meV. The results are plotted in Supplementary Fig.9.a-d. Each point of these curves can be seen as if the sample were in different initial conditions T_{eq} and $B_{t,eq}$. The results confirm the trends; indeed, the observed profiles are mostly monotonic and most of them do not change behavior (increase or decrease) with a change of the secondary parameter: B_t for the T-dependency (subfigures a-b) and T for the B_t-dependency (subfigures c-d). Interestingly, the central energy $< E >$ as a function of the temperature displays a different behavior depending on B_t: $< E >$ decreases with T if $B_t \lesssim 0.25$ but $< E >$ increases with T if $B_t \gtrsim 0.35$. As matter of fact, we know that the central energy of the d-d transitions should decrease when increasing the sample temperature. Thus, it gives us a range of validity of the model and, in the following, we choose $B_{t,eq} = 0.1$ to respect this experimental evidence. As explained in the main text, we are particularly interested in comparing the impact of a temperature variation around an equilibrium value T_{eq} in relation to the effects of a displacement variation around an equilibrium $B_{t,eq}$. Thus, we have studied the trend of the central energy and the energy bandwidth as a function of different variations of the temperature (Supplementary Fig.10.a-b) or as a function of the displacement (Supplementary Fig.10.c-d)) around some experimentally relevant parameters: $M = \omega = 16$ meV, $T_{eq} = 300$ K, $B_{t,eq} = 0.1$. As it is shown by all the figures, the trend is rather linear for positive or negative variations of the parameters δT and ΔB_t. The logarithm scale allows to better estimate $\Delta < E >$ or $\Delta\sigma_E$ as a function of δT or ΔB_t. In particular, we can observe that the retrieved $\Delta < E >$ or $\Delta\sigma_E$ for $\delta T = 10^{-2}$ K is one to two order of magnitude lower than the retrieved variation for $\Delta B_t = 10^{-3}$, which would be equivalent to a pump-induced displacement of 10^{-4}Å. This again demonstrates that the displacement variation around an equilibrium condition has a major role to play in the subsequent dynamical variations of the d-d transitions electronic properties. Note that the computation of these variations at $T_{eq} = 8$ K confirms this trend (taking into account $\delta T = 1$ K and $\Delta B_t = 10^{-3}$).

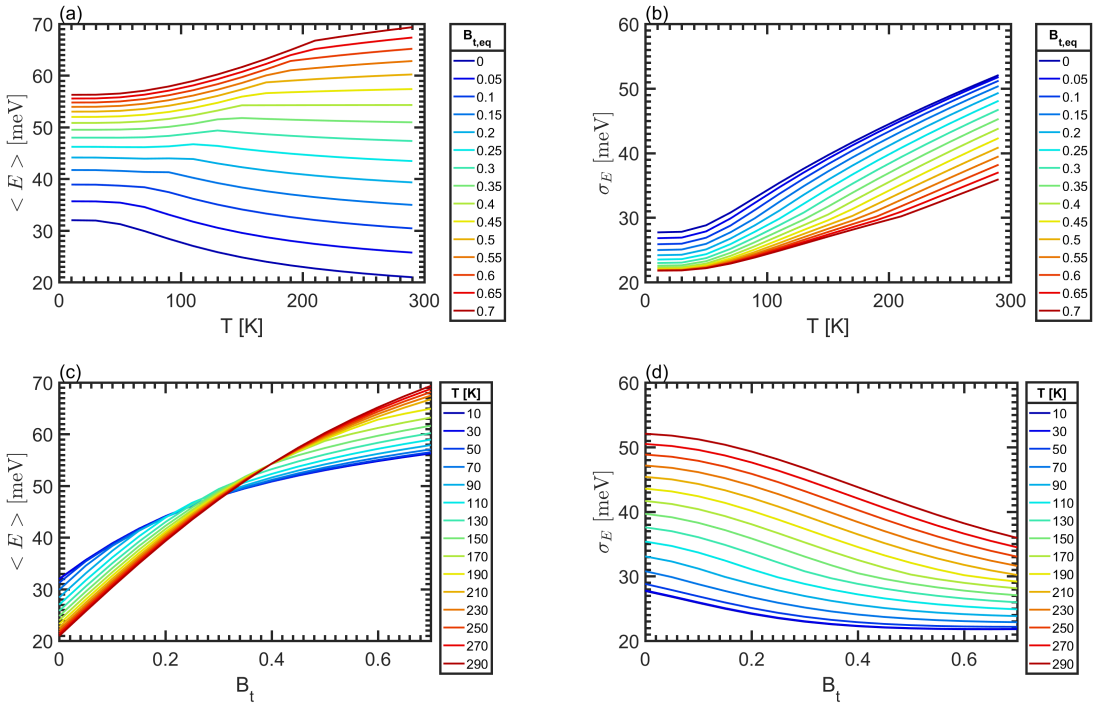

Figure 9: Central energy as a function of (a) the temperature and (c) the displacement. Energy bandwidth as a function of (b) the temperature and (d) the displacement. In each graph, a given color corresponds to a given secondary parameter: B_t for a-b and T for c-d.

3.4 Molecular electronic excitations

In our model we considered an interaction Hamiltonian between the light and the sample that is proportional to the phonon position operator $b+b^\dagger$. In order to justify this choice we recall here some basic notions of molecular physics.
Consider the wave function of a molecule in the Born-Oppenheimer approximation

$$\Phi_{\ell\nu}(r,R) = \psi_\ell(r;R)\chi_{\nu,\ell}(R), \tag{60}$$

where the electronic wave function $\psi_\ell(r;R)$ is a solution of the clamped-nuclei Schrödinger equation and depends parametrically on R, and the nuclear wave function $\chi_{\nu,\ell}(R)$ is the $\nu-th$ level eigenfunction relative to the harmonic potential corresponding to level ℓ.
The transition probability rate between two electronic states, labeled by $\ell = 0$ and $\ell = 1$, and vibrational levels $n \to m$, can be computed according to the Fermi Golden rule and reads

$$\Gamma_{0\to1}(\omega) = |\langle \nu = m, \ell = 1|\mu|\nu = n, \ell = 0\rangle|^2 \delta(\omega - E_{m-n}), \tag{61}$$

where the energy of the transition is $E_{m-n} = \epsilon + \omega_0(m-n)$ and the operator $\mu = eZ \cdot R - er = \mu_{el}(r) + \mu_{nu}(R)$ is the electric dipole moment containing both nuclear and electronic coordinates. The

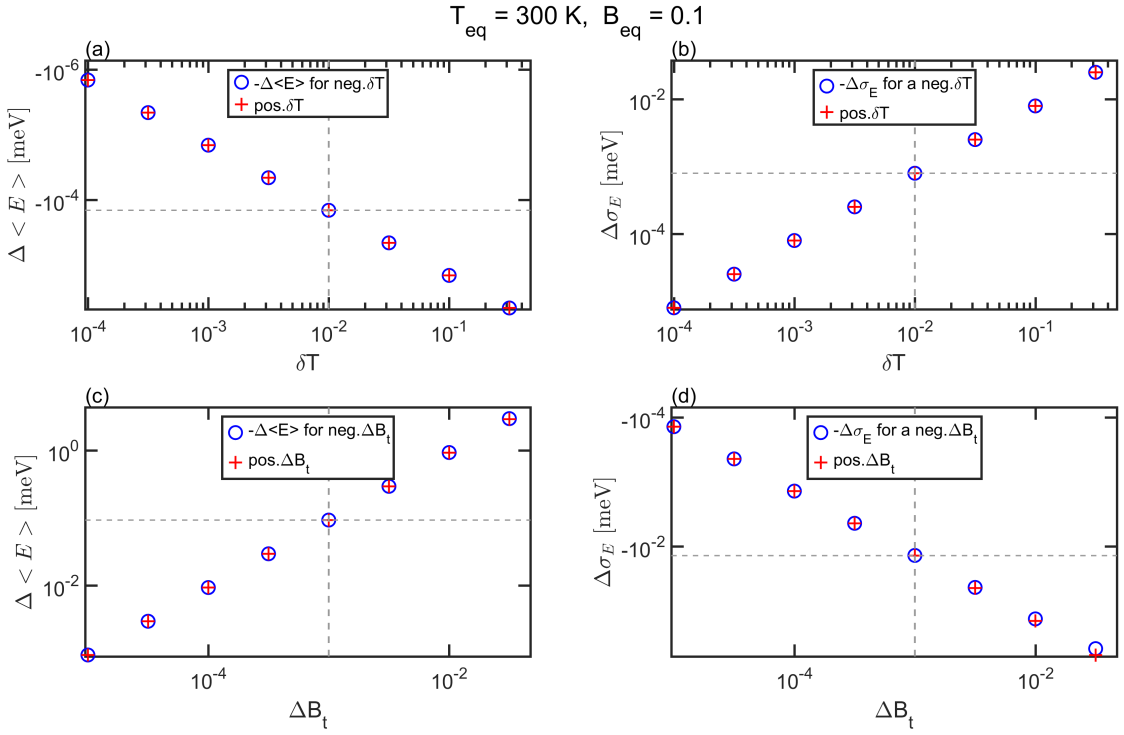

Figure 10: Central energy shift as a function of (a) the temperature and (c) the displacement. Energy bandwidth shift as a function of (b) the temperature and (d) the displacement. Positive parameter variations are represented by red cross and in the case of a negative parameter variation, the opposite of the computed shift is plotted as a function of the absolute value of the variation (blue circle).

matrix element reads

$$\begin{aligned}\langle \nu = m, \ell = 1 | \mu | \nu = n, \ell = 0 \rangle &= \int \mathrm{d}R\, \mathrm{d}r\, \psi_1^*(r;R) \chi_{m,1}^*(R)(\mu) \psi_0(r;R) \chi_{n,0}(R) \\ &= \int \mathrm{d}R \chi_{m,1}^*(R)\, \mu_{nu}(R)\, \chi_{n,0}(R) \int \mathrm{d}r \psi_1^*(r;R) \psi_0(r;R) + \\ &+ \int \mathrm{d}R \chi_{m,1}^*(R)\, \chi_{n,0}(R) \int \mathrm{d}r \psi_1^*(r;R) \mu_{el}(r) \psi_0(r;R). \end{aligned} \tag{62}$$

The first term is vanishing because the electronic wave functions form an orthonormal basis in the electronic Hilbert space for each fixed position of the nuclei R. For the same reason, we can expand a generic $\psi_n(r;R)$ in terms of the wave functions at the equilibrium position $\psi_m(r;R_0)$

$$\psi_n(r;R) = \sum_m c_{nm}(R - R_0) \psi_m(r;R_0). \tag{63}$$

For later convenience, we can define the integral

$$I_{mn} := \int \mathrm{d}r \psi_m^*(r;R_0) \mu_{el}(r) \psi_n(r;R_0). \tag{64}$$

Using this notation, the integral over the electronic coordinates in the second term of (62) becomes

$$\int \mathrm{d}r\psi_1^*(r;R)\mu_{el}(r)\psi_0(r;R) = c_{11}^* c_{00} I_{10} + \sum_{m\neq 1} c_{1m}^* c_{00} I_{m0} + \\ + \sum_{n\neq 0} c_{11}^* c_{0n} I_{1n} + \sum_{m\neq 1, n\neq 0} c_{1m}^* c_{0n} I_{mn}. \tag{65}$$

If the bare electronic transition is allowed by symmetry selection rules, then the first term I_{10} is the dominant contribution to the matrix element. On the contrary, if symmetry forbids the transition in equilibrium, namely $I_{10} = 0$, the other contributions become relevant [14, 18]. In particular, for small displacement from the equilibrium position we can expand the coefficients c in a Taylor series

$$c_{nn} = 1 + \alpha_n (R - R_0) + O((R - R_0)^2), \\ c_{nm} = \alpha_{nm}(R - R_0) + O((R - R_0)^2), \quad m \neq n$$

with some complex parameters α. The dominant terms in (65) are then

$$\int \mathrm{d}r\psi_1^*(r;R)\mu_{el}(r)\psi_0(r;R) \simeq (R - R_0)\left(\sum_{m\neq 1} \alpha_{1m}^* I_{m0} + \sum_{n\neq 0} \alpha_{0n} I_{1n}\right). \tag{66}$$

Coming back to the full expression for the matrix element (62) we get

$$\langle \nu = m, l = 1|\mu|\nu = n, l = 0\rangle = \left(\sum_{m\neq 1} \alpha_{1m}^* I_{m0} + \sum_{n\neq 0} \alpha_{0n} I_{1n}\right) \times \int \mathrm{d}R \chi_{m,1}^*(R)(R - R_0)\chi_{n,0}(R). \tag{67}$$

Therefore, our model is consistent with the previous findings, because the height of the spectral lines is proportional to the modulus squared of the following matrix element

$$\langle m|\mathrm{e}^{\frac{M}{\omega}(b^\dagger - b)}(b + b^\dagger)|n\rangle. \tag{68}$$

3.5 Relevant length scale estimation

In order to estimate the relevant length scale in our model, we consider a displaced harmonic potential of the form

$$V = \frac{1}{2} m\omega^2 x^2 + \lambda x, \tag{69}$$

where ω is the frequency, m is the mass of the oscillator and λ represents the coupling. In natural units ($c = \hbar = k_b = 1$), mass and frequency have the same physical units of energy, say eV, while the position x is expressed in eV^{-1}. For dimensional consistency λ has units of eV^2. The minimum of the harmonic trap V_{min} and the corresponding position x_{min} are

$$x_{min} = -\frac{\lambda}{m\omega^2}, \quad V_{min} = -\frac{1}{2}\frac{\lambda^2}{m\omega^2}. \tag{70}$$

By comparing the energy shift with the calculation done in the manuscript we can infer the relation between λ and M

$$\lambda = \sqrt{2m\omega} M, \tag{71}$$

and rewrite the position of the minimum in terms of M

$$x_{min} = -\frac{M}{\omega}\frac{\sqrt{2}}{\sqrt{m\omega}}. \tag{72}$$

This is also consistent with the evaluation of the average position in the displaced ground state computed using the quantum model

$$x_{ground} = \frac{1}{\sqrt{2m\omega}}\langle b + b^\dagger \rangle = -2\frac{M}{\omega}\frac{1}{\sqrt{2m\omega}} = -\frac{M}{\omega}\frac{\sqrt{2}}{\sqrt{m\omega}}. \tag{73}$$

In order to get numerical values for the quantity x_{min} we assume $\omega = 16meV$ and consider the mass of Copper as reference $m = 63.546\, a.m.u. = 5.9 \cdot 10^{10} eV$.
It turns out that

$$\frac{\sqrt{2}}{\sqrt{m\omega}} \simeq 0.46 \cdot 10^{-4} eV^{-1} \tag{74}$$

and using the conversion factor $1eV^{-1} = 1.97 \cdot 10^{-7} m$ we can find the connection between the physical displacement Δx and the adimensional parameter $\frac{M}{\omega}$

$$\Delta x \sim \frac{M}{\omega} \cdot 0.9 \cdot 10^{-11}\, m = \frac{M}{\omega} 0.09 \text{Å}. \tag{75}$$

The role of B_t is analogous to that of M/ω in the previous equation.

4 DFT calculation

We support our interpretation of the experimental observations using DFT (Density Functional Theory) simulations of the sample $CuGeO_3$. In particular, after obtaining the optimized structure we compared the ground state properties (band structure, insulating gap, antiferromagnetism of Cu chains) with the existing literature. Finally, we performed the calculation of the phonon modes of the crystal and computed the force field on the octahedron by displacing the atoms along the mode B_{2u} (see Methods for details).

4.1 Ground state calculations

The obtained band structures (Supplementary Fig.11.a and Supplementary Fig.11.b) are compatible and in turn they are in agreement with the result presented in [19]. Moreover, the spin-polarized calculation correctly converges to a solution with a finite atomic magnetic moment between $0.52\,\mu_B$ (QE) and $0.66\,\mu_B$ (octopus) in the antiferromagnetic Cu chain that is a bit lower than $0.76\,\mu_B$, the value found in [19]. However, the different methods that are used there can justify this mismatch.

4.2 Phonons

The calculation of the phonon modes has been performed with the software QE. The diagonalization of the dynamical matrix has been performed without the Hubbard correction because this function is currently not available in the software. The result is shown in the Table 1.
The remaining force field, which is computed by the sum of the force fields for opposite displacements, is detailed in Table 2 and it shows that the apical oxygen atoms are forced to move along the y direction as it is depicted in Figure 1.(c).

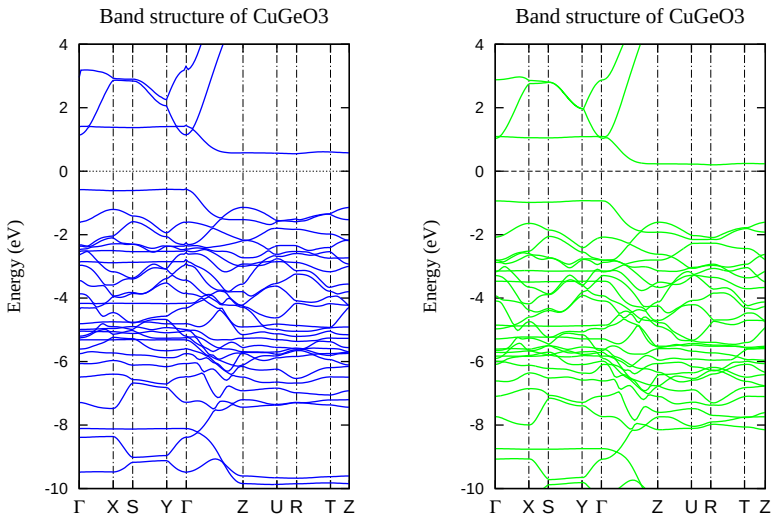

Figure 11: (a) Band structure of Copper Germanate obtained with octopus, using a spin-polarized PBE+U calculation, with pseudo-dojo pseudopotentials. A U value of 6.7 eV has been considered in order to compare results with [19]. (b) Band structure of Copper Germanate obtained with QE, using a spin-polarized PBE+U calculation, with pseudodojo pseudopotentials. A U value of 6.7 eV has been considered in order to compare results with [19].

Table 1: Phonon modes retrieved with QE.

frequency (cm^{-1})	symmetry	IR vs R	frequency (cm^{-1})	symmetry	IR vs R
-41.9	B_{3u}	I	289.5	A_g	R
-22.8	B_{2u}	I	341.8	B_{1u}	I
31.9	B_{1u}	I	366.3	B_{2g}	R
60.2	B_{1u}	I	377.3	B_{3g}	R
79.9	A_u		395.1	B_{1g}	R
115.4	B_{1g}	R	547.7	A_u	
120.0	B_{2g}	R	550.5	B_{2u}	I
124.7	B_{3u}	I	582.2	A_g	R
157.6	B_{2u}	I	586.6	B_{3u}	I
178.4	A_g	R	686.3	B_{1u}	I
191.0	B_{1u}	I	700.5	B_{1g}	R
224.0	B_{2g}	R	702.6	B_{2u}	I
262.2	B_{3u}	I	733.7	B_{2g}	R
272.2	B_{1u}	I	745.2	B_{3u}	I
284.8	B_{3u}	I	781.6	A_g	R

Table 2: Remaining force field acting on atoms (cartesian axes, Ry/au) and resulting from sum of the force fields for a positive ($+\Delta_x$) and a negative ($-\Delta_x$) displacement.

Atom	Type	ΔF_x	ΔF_y	ΔF_z
1	O	-2.7e-07	-0.00026	-0.000122
2	O	-2.7e-07	0.00026	0.000122
3	O	-2.2e-07	-0.00026	0.000119
4	O	-2.2e-07	0.00026	-0.000119
5	O	2.9e-07	-0.03425	1.4e-06
6	O	2.9e-07	0.03425	-1.4e-06
7	Cu	-2.7e-07	0	0
8	Cu	-4.3e-07	0	0
9	Ge	5.5e-07	0.03318	5.6e-06
10	Ge	5.5e-07	-0.03318	-5.6e-06

References

[1] M. Hase, I. Terasaki, and K. Uchinokura. Observation of the spin-peierls transition in linear Cu^{2+} (spin-2) chains in an inorganic compound cugeo$_3$. *Phys. Rev. Lett.*, 70:3651, 1993.

[2] A. Damascelli, D. van der Marel, G. Dhalenne, and A. Revcolevschi. Optical spectroscopy of pure and doped cugeo$_3$. *Phys. Rev. B*, 61:12063–12074, May 2000.

[3] Popovic Z. V. Phonons in $CuGeO_3$ studied using polarized far-infrared and raman-scattering spectroscopies. *Phys. Rev. B*, 52:4185, 1995.

[4] K. R. O'Neal, A. al Wanish, Z. Li, P. Chen, J. W. Kim, S.-. Cheong, G. Dhalenne, A. Revcolevschi, X.-T. Chen, and J. L. Musfeldt. Vibronic coupling and band gap trends in $CuGeO_3$ nanorods. *Phys. Rev. B*, 96:075437, 2017.

[5] C. Giannetti, G. Zgrablic, C. Consani, A. Crepaldi, D. Nardi, G. Ferrini, G. Dhalenne, A. Revcolevschi, and F. Parmigiani. Disentangling thermal and nonthermal excited states in a charge-transfer insulator by time- and frequency-resolved pump-probe spectroscopy. *Phys. Rev. B*, 80:235129, 2009.

[6] Y. Yuasa, M. Nakajima, T. Yamanouchi, Y. Ueda, and T. Suemoto. Ultrafast time-resolved spectroscopy of the spin-peierls compound $CuGeO_3$. *J. of Luminescence*, 128:1087, 2008.

[7] X. Liu, J. Wosnitza, H.v. Lohneysen, and R.K. Kremer. Specific heat of the spin-peierls compound $CuGeO_3$. *Z. Phys. B*, 98:163–165, 1995.

[8] M. Weiden, J. Kiihler, G. Sparn, M. Kiippen, M. Lang, C. Geibel, and F. Steglich. Thermodynamic properties of the spin-peierls transition in $CuGeO_3$. *Z. Phys. B*, 98:167–169, 1995.

[9] J. Zeman, G. Martinez, P. H. M. van Loosdrecht, G. Dhalenne, and A. Revcolevschi. Scaling of the h-t phase diagram of $CuGeO_3$. *Phys. Rev. Lett.*, 83:2648, 1999.

[10] M. Bassi, P. Camagni, R. Rolli, G. Samoggia, F. Parmigiani, G. Dhalenne, and A. Revcolevschi. Optical absorption of $CuGeO_3$. *Phys. Rev. B*, 54:R11 0030, 1996.

[11] A. Cartella. *Amplification of optically driven phonons.* PhD thesis, 2017.

[12] A. Taflove and S. C. Hagness. *Computational electrodynamics : the finite-difference time-domain method.* Boston, MA : Artech House, 2005.

[13] G. D. Mahan. *Many-Particle Physics.* Third Edition (Springer), 2000.

[14] B. H. Bransden and C. J. Joachain. *Physics of Atoms and Molecules.* Pearson Education, 2003.

[15] C. J. Ballhausen. *Ligand Field Theory.* McGraw-Hill, New York,, 1962.

[16] I. S. Gradshteyn and I. M. Ryzhik. *Table of Integrals, Series, and Products.* Seventh Edition, (Academic Press), 2007.

[17] Filippo Glerean, Stefano Marcantoni1, Giorgia Sparapassi, Andrea Blason, Martina Esposito, Fabio Benatti1, and Daniele Fausti. Quantum model for impulsive stimulated raman scattering. *J. Phys. B: At. Mol. Opt. Phys.*, 52:145502, 2019.

[18] W. Demtröder. *Atoms, Molecules and Photons*. Springer, 2006.

[19] Hua Wu, Mei chun Qian, and Qing qi Zheng. Insulating band structure of. *Journal of Physics: Condensed Matter*, 11(1):209–219, jan 1999.